

Holographic analysis of colloidal spheres sedimenting in horizontal slit poresLauren E. Altman  and David G. Grier *Department of Physics and Center for Soft Matter Research, New York University, New York, New York 10003, USA*

(Received 3 August 2022; accepted 27 September 2022; published 17 October 2022)

The mobility of a colloidal particle in a slit pore is modified by the particle's hydrodynamic coupling to the bounding surfaces and therefore depends on the particle's position within the pore and its direction of motion. We report holographic particle tracking measurements of colloidal particles' diffusion and sedimentation between parallel horizontal walls that yield the mobility for motions perpendicular to the walls, including its dependence on height within the channel. These measurements complement previous studies that probed colloidal mobility parallel to confining surfaces. When interpreted with effective-medium theory, holographic characterization measurements yield estimates for the sedimenting spheres' densities that can be compared with kinematic values to draw insights into the spheres' compositions. This comparison suggests, for example, that the silica spheres used in this study are slightly porous, but that their pores are too small for water to penetrate.

DOI: [10.1103/PhysRevE.106.044605](https://doi.org/10.1103/PhysRevE.106.044605)**I. INTRODUCTION**

Colloidal particles are coupled to each other and to the walls of their containers by hydrodynamic interactions. Hydrodynamic coupling modifies how colloidal particles respond to external forces and collectively contributes to their dispersions' rheological properties. Developing analytical expressions for colloidal particles' mobility is impractical for all but the simplest systems. Here, we revisit one such archetypal system comprised of a single colloidal sphere confined to the gap between two rigid horizontal planar walls.

Previous experimental studies have used dynamic light scattering [1], multiple light scattering [2], and conventional video microscopy [3–5] to measure the mobility of colloidal spheres confined by parallel walls. Light scattering techniques, however, average over the height of the channel and so do not probe how the particle's mobility varies with its position in the channel. The limited depth of focus of conventional microscopy similarly has prevented particle-tracking studies from assessing the full position dependence of the mobility [4,5]. Dynamic stereo microscopy has been used to track micrometer-scale colloidal spheres sedimenting onto a single horizontal surface [6]. The particles' radii in such imaging measurements are estimated indirectly by analyzing thermal fluctuations or are treated as adjustable parameters. The resulting lack of precision in particle size limits how much information can be extracted about the particles' coupling to the surrounding fluid and bounding surfaces.

The present study rounds out the experimental literature on this canonical system by measuring how a sphere's mobility perpendicular to the parallel walls of a rectangular channel depends on its height within the channel. These measurements use holographic video microscopy to track individual spheres' three-dimensional motions with nanometer-scale precision as they freely sediment from the top wall of the channel to the bottom. Spheres are reproducibly positioned at the top wall using holographic optical traps.

We interpret the results of these measurements with an implicit formulation of the sphere's trajectory in the linear superposition approximation. The result is parametrized by the sphere's radius relative to the channel depth and by the sphere's buoyant mass density. Holographic tracking has the advantage over other techniques of directly measuring the sphere's radius with nanometer precision. The wall separation consequently can be inferred from the measured trajectory. Holographic microscopy therefore provides a kinematic estimate for the sedimenting sphere's density.

Holographic characterization also yields the sphere's refractive index with part-per-thousand precision. Effective-medium theory then provides an independent estimate of the sphere's density. Comparisons between kinematic and holographic density estimates offer useful insights into the sphere's composition while also serving to validate the effective-sphere interpretation of holographic characterization data [7,8].

II. LORENZ MIE MICROSCOPY

Figure 1(a) schematically represents the measurement system. A beam of collimated laser light with vacuum wavelength λ and frequency ω illuminates a colloidal particle dispersed in a fluid medium of refractive index n_m . The electric field of this beam may be modeled as a plane wave polarized along \hat{x} and propagating along the vertical \hat{z} axis,

$$\mathbf{E}_0(\mathbf{r}) = u_0 e^{ikz} e^{-i\omega t} \hat{x}. \quad (1)$$

Here, u_0 is the beam's amplitude and $k = 2\pi n_m/\lambda$ is the wave number of light in the medium. Our implementation uses a fiber-coupled diode laser (Coherent Cube) operating at $\lambda = 447$ nm. The 10 mW beam is collimated at 3 mm diameter, which more than fills the input pupil of an objective lens (Nikon Plan Apo, 100 \times , numerical aperture 1.4, oil immersion). In combination with a 200 mm tube lens, this objective

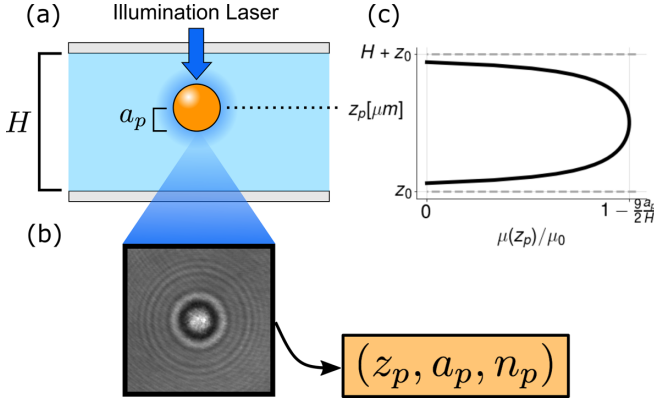


FIG. 1. Schematic representation of the holographic sedimentation measurement. (a) A colloidal sphere with radius a_p is confined to a channel of width H . The sphere is illuminated with a collimated laser beam as it moves through the channel in three dimensions. (b) Light scattered off of the sphere interferes with the rest of the illumination to produce a hologram. This hologram may be interpreted with Lorenz-Mie theory to yield simultaneous measurements of a_p , the sphere's axial position, z_p , and the sphere's refractive index, n_p . (c) The sphere's hydrodynamic mobility μ depends on its axial position z_p according to Eq. (7) due to hydrodynamic coupling to the walls.

relays images to a gray scale camera (FLIR Flea3 USB 3.0) with a $1280 \text{ pixel} \times 1024 \text{ pixel} \times \text{el sensor}$, yielding a system magnification of 48 nm/pixel .

A colloidal particle located at \mathbf{r}_p relative to the center of the microscope's focal plane scatters a small proportion of the illumination to position \mathbf{r} in the focal plane of the microscope,

$$\mathbf{E}_s(\mathbf{r}) = E_0(\mathbf{r}_p) \mathbf{f}_s(k(\mathbf{r} - \mathbf{r}_p)). \quad (2)$$

The scattered wave's relative amplitude, phase, and polarization are described by the Lorenz-Mie scattering function, $\mathbf{f}_s(k\mathbf{r})$, which generally depends on the particle's size, shape, orientation, and composition. For simplicity, we model the particle as an isotropic homogeneous sphere, so that $\mathbf{f}_s(k\mathbf{r})$ depends only on the particle's radius, a_p , and its refractive index, n_p [9–11].

The microscope magnifies the interference pattern formed by the superposition of incident and scattered waves and the camera records its intensity. Each snapshot in the camera's video stream constitutes a hologram of the particles in the observation volume. The image in Fig. 1(b) shows a typical hologram of a colloidal silica sphere recorded at $\lambda = 447 \text{ nm}$ with a system magnification of 48 nm/pixel .

The distinguishing feature of Lorenz-Mie microscopy is how it extracts information from recorded holograms. Rather than using diffraction integrals to reconstruct the volumetric light field responsible for the recorded hologram, Lorenz-Mie microscopy instead treats the analysis as an inverse problem, modeling the hologram as [12]

$$I(\mathbf{r}) = u_0^2 |\hat{x} + e^{-ikz_p} \mathbf{f}_s(k(\mathbf{r} - \mathbf{r}_p))|^2 + I_0, \quad (3)$$

where I_0 is the calibrated dark count of the camera. Fitting Eq. (3) to a measured hologram yields the particle's three-dimensional position, $\mathbf{r}_p = (x_p, y_p, z_p)$, as well as its radius, a_p , and its refractive index, n_p , at the imaging

wavelength. Lorenz-Mie measurements on micrometer-scale spheres typically yield tracking and characterization results with exceptionally good precision [7]. The uncertainties in the in-plane coordinates are $\sigma_{x_p} = \sigma_{y_p} = 2 \text{ nm}$ over a field of view extending to $100 \mu\text{m}$. The vertical coordinate is less well resolved, with an uncertainty of $\sigma_{z_p} = 5 \text{ nm}$ over a range of $100 \mu\text{m}$. The uncertainty in the radius is typically $\sigma_{a_p} = 2 \text{ nm}$ and the uncertainty in the refractive index is $\sigma_{n_p} = 0.001$.

III. HOLOGRAPHIC OPTICAL TRAPPING

We position colloidal spheres reproducibly within the channel with optical tweezers and then release them to track their motions. Our traps are created with the holographic optical trapping technique [13] using the microscope's objective lens to focus computer-generated phase-only holograms into the sample. The trapping system is powered by a fiber laser operating at a vacuum wavelength of 1064 nm (IPG Photonics YLR-10-LP) and uses a liquid-crystal spatial light modulator (Holoeye Pluto) to imprint holograms on the light's wave fronts. The modified beam is relayed into the objective lens with a dielectric multilayer dichroic mirror (Semrock), which permits simultaneous holographic trapping and holographic imaging.

Figure 2 presents the results from a typical holographic analysis of a silica sphere's sedimentation. This sphere is drawn from a commercial sample with a nominal radius of $a_p = 0.75 \mu\text{m}$ (Duke Standards, catalog no. 8150) and is dispersed in water. The sample is confined to the gap between a glass microscope slide and a glass no. 1.5 coverslip whose edges are bonded to the slide with optical adhesive (Norland NOA68). The separation between the inner glass surfaces is set to roughly $H \approx 20 \mu\text{m}$ by capillary forces before the cell is sealed.

Figure 2(a) shows the sphere's axial position as a function of time, measured at 24 frames^{-1} . Fluctuations in $z_p(t)$ reflect the sphere's Brownian motion; measurement errors are too small to see at the scale of the plot. The discrete points in Fig. 2(b) reflect values for the sphere's radius and refractive index obtained at each time step and are colored by the density of observations, $P(a_p, n_p)$. The mean value for the refractive index, $n_p = 1.433(9)$, is consistent with expectations for slightly porous silica [14]. We use the trajectory-averaged radius, $a_p = 0.814 \pm 0.007 \mu\text{m}$, to interpret the results. For example, the plateaus in $z_p(t)$ at the beginning and end of the trajectory correspond to the particle being pressed against the upper wall of the channel by the optical tweezer and sitting against the lower wall due to gravity, respectively. Given the measured particle radius, we therefore can estimate the positions of the upper and lower walls of the channel, which are indicated by the horizontal dashed lines in Fig. 2(a).

IV. CONFINED SEDIMENTATION

A small dense sphere sediments through a viscous fluid under the influence of gravity at a rate

$$\frac{dz_p}{dt} = -\mu(z_p) \Delta m_p g \quad (4a)$$

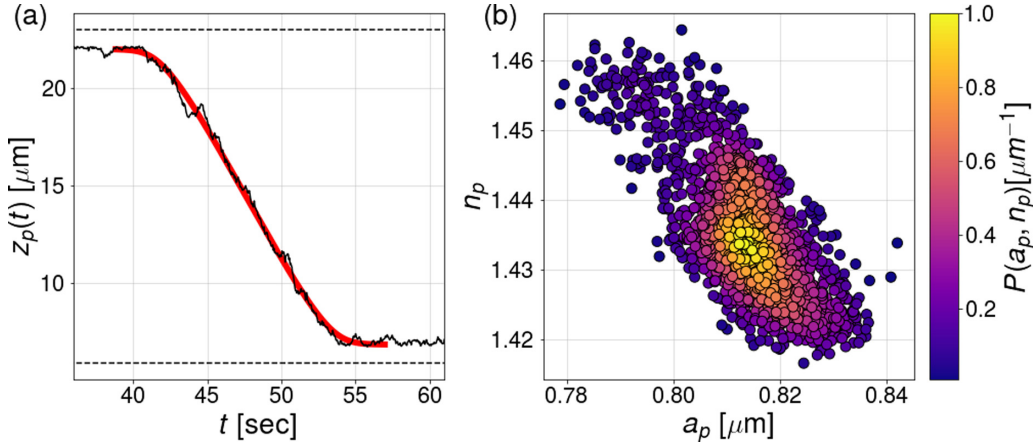


FIG. 2. Simultaneous holographic measurements of (z_p, a_p, n_p) for a $1.5 \mu\text{m}$ diameter silica sphere as it sediments between two walls. (a) The particle's trajectory $z_p(t)$ (black) is fitted to Eq. (12) to obtain the red curve and hydrodynamic estimates for the positions of each wall, $z_0 = 6.1 \mu\text{m}$, $H = 16.9 \mu\text{m}$, as well as the buoyant mass of the particle, Δm_p , which may be interpreted to determine its hydrodynamic density, $\rho_H = 2.05(3)e3 \text{ kg/m}^3$, using holographic estimates of its radius. (b) Measurements of a_p and n_p at each time step yield trajectory-averaged values of $a_p = 0.814 \pm 0.007 \mu\text{m}$ and $n_p = 1.433(9)$. Applying effective-medium theory to these values yields an independent estimate for the particle's density, $\rho_p = 2.06(4)e3 \text{ kg/m}^3$, assuming the particle's pores to be empty.

that depends on its position-dependent mobility, $\mu(z_p)$, the acceleration due to gravity, g , and the sphere's buoyant mass,

$$\Delta m_p = \frac{4}{3}\pi a_p^3 (\rho_p - \rho_m), \quad (4b)$$

where ρ_p and ρ_m are the mass densities of the particle and the medium, respectively. Equation (4a) neglects inertial effects under the assumption that the motion is overdamped, which is reasonable for micrometer-scale colloidal spheres in water.

The mobility of a sphere moving through an unbounded fluid with viscosity η is given by the Stokes formula,

$$\mu_0 = \frac{1}{6\pi\eta a_p}. \quad (5)$$

Confining the sphere within a channel reduces its mobility through hydrodynamic coupling to the walls. The mobility depends both on the sphere's height, z_p , within the channel and also on the direction of motion. The mobility for a sphere moving toward a rigid horizontal surface is well approximated by Faxén's result [15]

$$\frac{\mu(h)}{\mu_0} = 1 - \frac{9}{8} \frac{a_p}{h} + \frac{1}{2} \frac{a_p^3}{h^3} + \mathcal{O}\left\{\frac{a_p^4}{h^4}\right\}, \quad (6)$$

where $h = z_p - z_0$ is the sphere's height above a wall located at z_0 along \hat{z} .

Coupling to a pair of parallel walls is far more complicated because of the need to satisfy no-flow boundary conditions on both rigid surfaces [16]. Provided the sphere does not fill too large a proportion of the channel's wall-to-wall separation, H , the mobility can be approximated with Oseen's linear superposition approximation [4,8,15],

$$\frac{\mu(z_p)}{\mu_0} \approx 1 - \frac{9}{8} \frac{a_p}{z_p - z_0} - \frac{9}{8} \frac{a_p}{H - z_p + z_0}. \quad (7)$$

This functional form is plotted in Fig. 1(c). Equation (7) has been found to agree quantitatively with numerical solutions to the Navier-Stokes equation for $a_p/H \ll 0.1$ [17].

Using Eq. (7) for the confined sphere's mobility, Eq. (4a) can be recast into dimensionless form,

$$\frac{d\zeta}{d\tau} = \frac{\alpha^2 - \zeta^2}{1 - \zeta^2}, \quad (8)$$

by defining the dimensionless position,

$$\zeta = 2 \frac{z_p - z_0}{H} - 1, \quad (9)$$

the dimensionless time,

$$\tau = \mu_0 \Delta m_p g \frac{2}{H} (t - t_0), \quad (10)$$

relative to the time, t_0 , that the particle reaches the midplane of the chamber, and a geometric parameter,

$$\alpha = \sqrt{1 - \frac{9}{2} \frac{a_p}{H}}. \quad (11)$$

The particle begins its trajectory at $\zeta = 1 - 2a_p/H$ and descends to height $\zeta(\tau)$ by time

$$\tau(\zeta) = \left(\alpha - \frac{1}{\alpha}\right) \operatorname{arctanh}\left(\frac{\zeta}{\alpha}\right) - \zeta, \quad (12)$$

which is obtained by integrating Eq. (8). The arrival time diverges when $\alpha \leq 0$ or $a_p \geq 0.22H$, which sets the domain of validity for Eq. (12). The former limit requires that the sphere be more dense than the medium. The latter is consistent with the linear superposition approximation for the mobility. For $a_p/H = 0.15$, corrections to $\mu(z_p)$ of order $(a_p/H)^3$ contribute a 10% correction to $\tau(\zeta)$.

The smooth (red) curve superimposed on the trajectory data in Fig. 2(a) is a three-parameter fit to Eq. (12) for the positions of the two walls of the chamber and the sphere's buoyant mass. The sphere's density is obtained from the buoyant mass using the holographically measured radius. Taking the density of water to be $\rho_m = 997 \text{ kgm}^{-3}$, the hydrodynamic estimate for the density of the sphere is $\rho_H = 2.05(3)e3 \text{ kgm}^{-3}$. This value is slightly smaller than the density of amorphous silica,

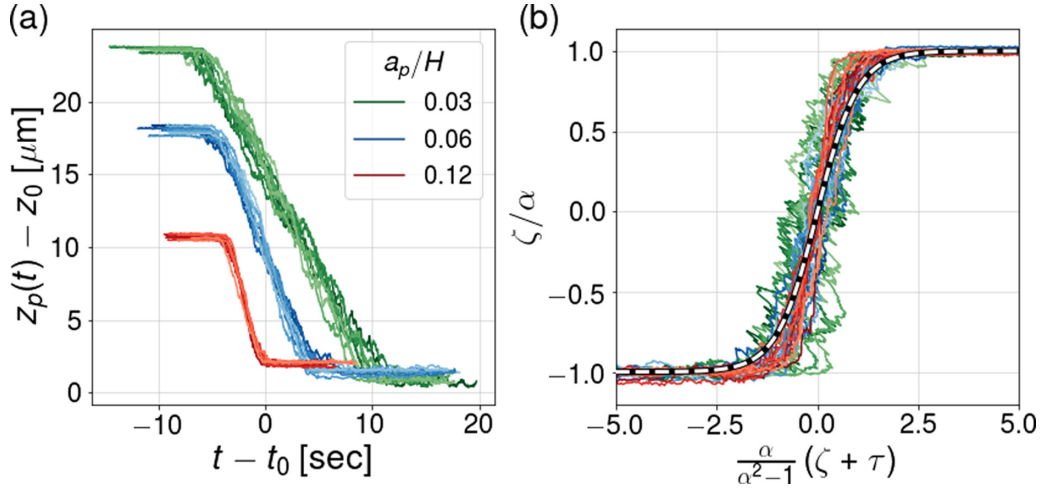


FIG. 3. Trajectories for three sizes of silica spheres sedimenting in three different channels. (a) Ten trajectories from each particle type: $a_p/H = 0.03$ (green), $a_p/H = 0.06$ (blue), and $a_p/H = 0.12$ (red). Trajectories from each particle type are shifted along t for readability. (b) Data collapse in the linear superposition approximation. The master curve from Eq. (15) is plotted as a dashed (white) curve superimposed on the data.

$\rho_0 = 2.2 \times 10^3 \text{ kgm}^{-3}$ [14,18], which suggests that the sphere is slightly porous.

Effective medium theory

The refractive index of a porous particle reflects properties of both the particle's base material and also the material filling its pores. Given a base material with refractive index n_0 , and assuming the pores are small, evenly dispersed throughout the particle, and filled with a material of refractive index n_1 , the porous particle's effective refractive index, n_p , is related by Maxwell Garnett effective-medium theory [19] to n_0 and n_1 by [20,21]

$$L\left(\frac{n_p}{n_m}\right) = \phi L\left(\frac{n_0}{n_m}\right) + (1 - \phi)L\left(\frac{n_1}{n_m}\right), \quad (13a)$$

where ϕ is the volume fraction of base material in the particle and where

$$L(m) = \frac{m^2 - 1}{m^2 + 2} \quad (13b)$$

is the Lorentz-Lorenz function.

Equation (13) can be used to estimate the particle's volume fraction, ϕ , from the holographically measured value of n_p together with *a priori* knowledge of n_0 and n_1 . This approach has been validated through studies on nanoporous colloidal spheres [7,20,21], fractal protein aggregates [22], fractal nanoparticle agglomerates [23,24], and dimers of spheres [25]. For the present study, $n_0 = 1.465$ is the refractive index of amorphous silica at $\lambda = 447 \text{ nm}$ [26] and $n_1 = n_m = 1.340$ if the pores are filled with water [27]. Alternatively, if the pores are too small or inaccessible to imbibe water [14] then $n_1 = 1$.

Given the volume fraction of the particle, its mass density follows from

$$\rho_p = \rho_0\phi + \rho_1(1 - \phi), \quad (14)$$

where ρ_1 is the mass density of the material in the pores. For a silica sphere dispersed in water, $\rho_0 = 2.2 \times 10^3 \text{ kgm}^{-3}$

[14,18] and $\rho_1 = \rho_m = 997 \text{ kgm}^{-3}$ if water permeates its pores. Alternatively, $\rho_1 = 0$ if the pores are empty.

Applying this result to the holographic characterization data in Fig. 2(b) yields an optical estimate for the sphere's mass density of $\rho_p = 1.90(9)e3 \text{ kgm}^{-3}$ if the pores are saturated with water. This value increases to $\rho_p = 2.06(4)e3 \text{ kgm}^{-3}$ if we assume instead that the pores are empty. The hydrodynamic estimate agrees with this value only if the pores are assumed to be empty. This is consistent with independent measurements performed with spin-echo small angle neutron scattering [28] and with helium and Gay-Lussac pycnometry [14], both of which suggest that the pores in Stöber-condensed silica spheres are too small or inaccessible for water to penetrate.

V. RESULTS

Figure 3(a) presents results from holographic sedimentation measurements on three different sizes of silica spheres in channels of different heights. The smallest spheres (green) have a nominal radius of $a_p = 0.84 \mu\text{m}$ (Duke Standards, catalog no. 8150) and are dispersed at a volume fraction of $10^{-7} \text{ particlesm}^{-1}\text{L}$ in a channel of height $H = 25 \mu\text{m}$, so that $a_p/H = 0.03$, which falls within the valid range for the linear superposition approximation. The intermediate-sized spheres (blue) at $a_p = 1.19 \mu\text{m}$ (Bangs Laboratories, catalog no. SS05000) are confined in a channel with $H = 19 \mu\text{m}$, yielding $a_p/H = 0.06$. The largest spheres (red) at $a_p = 1.54 \mu\text{m}$ (Bangs Laboratories, catalog no. SS05001) are confined in the narrowest channel, $H = 13 \mu\text{m}$. These particles fill a large enough fraction of the channel, $a_p/H = 0.12$, for deviations from the linear superposition approximation to become apparent. Each of the three data sets includes two independent experiments on each of five different spheres. The largest trajectory fluctuations are seen in the smallest spheres and can be ascribed to Brownian motion. Each data set is fit to Eq. (12) for Δm_p , z_0 , and H , using the holographically measured value of a_p to compute the geometric factor, α , using Eq. (11).

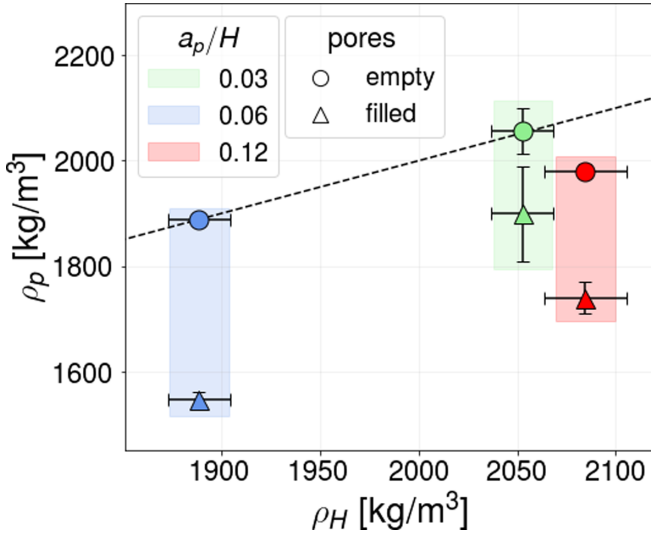


FIG. 4. Comparison of the estimates for hydrodynamic density, ρ_H , and optical density, ρ_p , for a representative particle from each of the three particle types. Limiting values of ρ_p are plotted for empty pores (circles: $n_1 = 1$, $\rho_1 = 0$) and filled pores (triangles: $n_1 = n_m$, $\rho_1 = \rho_m$). The dashed (black) line represents the identity $\rho_p = \rho_H$.

To the extent that the approximations underlying Eq. (7) are valid, trajectories of sedimenting spheres should fall on a master curve obtained by rearranging Eq. (12):

$$\frac{\zeta}{\alpha} = \tanh\left(\frac{\alpha}{\alpha^2 - 1}(\zeta + \tau)\right). \quad (15)$$

Figure 3(b) shows that all three data sets from Fig. 3(a) collapse onto the master curve when recast in this form. Brownian fluctuations cause sizable random deviations for the smallest particles (green). The trajectories of the most strongly confined particles (red) deviate systematically from the master curve near contact with the walls at $\zeta = \pm\alpha$ because of higher-order corrections to the spheres' hydrodynamic coupling to the walls.

Fitting to the hydrodynamic model yields an estimate, ρ_H , for the density of each sphere. Values of ρ_H are compared in Fig. 4 with optical estimates, ρ_p , obtained with Eqs. (13) and (14) assuming either that water is imbibed into the spheres' pores or not. The two estimates based on empty and filled pores represent the upper and lower bounds, respectively, of the mass density that can be inferred for these particles based on holographic characterization alone. Errors in the optical estimates are propagated from uncertainty in the refractive index of the spheres, while errors in the hydrodynamic estimates are dominated by uncertainty in the radii, which also are measured holographically. The dashed line in Fig. 4 represents agreement between hydrodynamic and optical estimates for the mass density. For this selection of silica spheres dispersed in water, the hydrodynamic density agrees most closely with the limiting case in which the pores are empty. This conclusion is consistent with independent measurements on similar systems performed with orthogonal measurement techniques [14,28]. This agreement serves to validate (1) the precision and accuracy of single particle characterization by holographic microscopy, (2) the reliability of the effective-medium interpretation of holographic characterization data,

and (3) the proposal that holographic characterization can be used to infer particles' mass densities without requiring dynamical measurements.

Success of the all-optical density measurement also validates the analytic result introduced in Eq. (12) for the trajectory of a sphere sedimenting in a horizontal slit pore. Specifically, the model yields reliable values for a particle's buoyant mass, and therefore its density, despite corrections to the mobility due to hydrodynamic coupling to the walls of the channel. As anticipated, the model accounts for this coupling for $a_p/H < 0.1$. The largest and most strongly confined spheres in our study fall outside that limit and therefore yield less satisfactory agreement between hydrodynamic and optical estimates for the density. We propose therefore that holographic particle characterization is a viable platform for single-particle densitometry and single-particle pycnometry, and that it complements conventional techniques because it can be applied to dissimilar particles in heterogeneous samples.

VI. DISCUSSION

Single-particle tracking by holographic microscopy provides the precision, range, and time resolution needed to study colloidal sedimentation in confined geometries such as slit pores. Reproducible measurements on selected particles are made possible by combining holographic microscopy with holographic optical trapping for noninvasive micromanipulation. We have used these capabilities to measure the mobility of individual micrometer-scale colloidal spheres in the direction perpendicular to plane parallel walls in a rectangular channel. These measurements complement previous experimental studies, which did not have access to individual particles' axial coordinates across the entire channel [3–5].

We interpret measurements of single-particle sedimentation with a model that incorporates hydrodynamic coupling to the walls through Faxén's lowest-order single-wall modification to the mobility together with Oseen's linear superposition approximation. This simplified model admits an analytic expression for a confined particle's trajectory that compares well with measurements, even for spheres that fill a substantial fraction of the channel. Fitting to the model yields an estimate for the particle's buoyant mass despite the influence of confinement.

In addition to three-dimensional tracking, holographic microscopy also measures the size and refractive index of each particle in the field of view. Precise holographic measurements of a particle's size can be used to estimate its mass density from its sedimentation velocity. When interpreted with effective-medium theory, a particle's holographically measured refractive index can be used to obtain an independent estimate for its mass density.

Comparing hydrodynamic measurements with optical estimates offers insights into the composition of the sedimenting particle. In the case of aqueous dispersions of silica spheres, this comparison suggests that the spheres are slightly porous but that the pores do not imbibe water, perhaps because they are too small or are not simply connected. This can be contrasted with the behavior of nanoporous silica spheres and branched fractal aggregates, whose pores are permeated with the surrounding fluid medium [21].

ACKNOWLEDGMENTS

This work was primarily supported by the SBIR program of the National Institutes of Health under Award No. R44TR001590. The Titan Xp GPU used for this work was

provided by a GPU Grant from nVidia. The custom holographic characterization instrument was constructed with support from the MRI program of the NSF under Award No. DMR-0922680.

-
- [1] L. Lobry and N. Ostrowsky, Diffusion of Brownian particles trapped between two walls: Theory and dynamic-light-scattering measurements, *Phys. Rev. B* **53**, 12050 (1996).
- [2] J.-Z. Xue, E. Herbolzheimer, M. A. Rutgers, W. B. Russel, and P. M. Chaikin, Diffusion, Dispersion, and Settling of Hard Spheres, *Phys. Rev. Lett.* **69**, 1715 (1992).
- [3] J. C. Crocker and D. G. Grier, Methods of digital video microscopy for colloidal studies, *J. Colloid Interface Sci.* **179**, 298 (1996).
- [4] E. R. Dufresne, D. Altman, and D. G. Grier, Brownian dynamics of a sphere between parallel walls, *Europhys. Lett.* **53**, 264 (2001).
- [5] B. Lin, J. Yu, and S. A. Rice, Direct measurements of constrained Brownian motion of an isolated sphere between two walls, *Phys. Rev. E* **62**, 3909 (2000).
- [6] M. P. Lee, G. M. Gibson, D. Phillips, M. J. Padgett, and M. Tassieri, Dynamic stereo microscopy for studying particle sedimentation, *Opt. Express* **22**, 4671 (2014).
- [7] B. J. Krishnatreya, A. Colen-Landy, P. Hasebe, B. A. Bell, J. R. Jones, A. Sunda-Meya, and D. G. Grier, Measuring Boltzmann's constant through holographic video microscopy of a single sphere, *Am. J. Phys.* **82**, 23 (2014).
- [8] L. E. Altman and D. G. Grier, CATCH: Characterizing and tracking colloids holographically using deep neural networks, *J. Phys. Chem. B* **124**, 1602 (2020).
- [9] C. F. Bohren and D. R. Huffman, *Absorption and Scattering of Light by Small Particles* (Wiley Interscience, New York, 1983).
- [10] M. I. Mishchenko, L. D. Travis, and A. A. Lacis, *Scattering, Absorption and Emission of Light by Small Particles* (Cambridge University Press, Cambridge, UK, 2001).
- [11] G. Gouesbet and G. Gréhan, *Generalized Lorenz-Mie Theories* (Springer-Verlag, Berlin, 2011).
- [12] S.-H. Lee, Y. Roichman, G.-R. Yi, S.-H. Kim, S.-M. Yang, A. van Blaaderen, P. van Oostrum, and D. G. Grier, Characterizing and tracking single colloidal particles with video holographic microscopy, *Opt. Express* **15**, 18275 (2007).
- [13] D. G. Grier, A revolution in optical manipulation, *Nature (London)* **424**, 810 (2003).
- [14] N. Plumeré, A. Ruff, B. Speiser, V. Feldmann, and H. A. Mayer, Stöber silica particles as basis for redox modifications: Particle shape, size, polydispersity, and porosity, *J. Colloid Interface Sci.* **368**, 208 (2012).
- [15] J. Happel and H. Brenner, *Low Reynolds Number Hydrodynamics* (Kluwer, Dordrecht, 1991).
- [16] N. Liron and S. Mochon, Stokes flow for a stokeslet between two parallel flat plates, *J. Eng. Math.* **10**, 287 (1976).
- [17] H. Power and B. F. de Power, Second-kind integral equation formulation for the slow motion of a particle of arbitrary shape near a plane wall in a viscous fluid, *SIAM J. Appl. Math.* **53**, 60 (1993).
- [18] O. V. Mazurin, M. V. Streltsina, and T. P. Shvaiko-Shvaikovskaya, *Silica Glass and Binary Silicate Glasses* (Elsevier, Amsterdam, 2012).
- [19] V. Markel, Introduction to the Maxwell Garnett approximation: tutorial, *J. Opt. Soc. Am. A* **33**, 1244 (2016).
- [20] F. C. Cheong, K. Xiao, D. J. Pine, and D. G. Grier, Holographic characterization of individual colloidal spheres' porosities, *Soft Matter* **7**, 6816 (2011).
- [21] M. A. Odete, F. C. Cheong, A. Winters, J. J. Elliott, L. A. Philips, and D. G. Grier, The role of the medium in the effective-sphere interpretation of holographic particle characterization data, *Soft Matter* **16**, 891 (2020).
- [22] C. Wang, X. Zhong, D. B. Ruffner, A. Stutt, L. A. Philips, M. D. Ward, and D. G. Grier, Holographic characterization of protein aggregates, *J. Pharm. Sci.* **105**, 1074 (2016).
- [23] C. Wang, F. C. Cheong, D. B. Ruffner, X. Zhong, M. D. Ward, and D. G. Grier, Holographic characterization of colloidal fractal aggregates, *Soft Matter* **12**, 8774 (2016).
- [24] J. Fung and S. Hoang, Computational assessment of an effective-sphere model for characterizing colloidal fractal aggregates with holographic microscopy, *J. Quant. Spectrosc. Radiat. Transfer* **236**, 106591 (2019).
- [25] L. E. Altman, R. Quddus, F. C. Cheong, and D. G. Grier, Holographic characterization and tracking of colloidal dimers in the effective-sphere approximation, *Soft Matter* **17**, 2695 (2021).
- [26] I. H. Malitson, Interspecimen comparison of the refractive index of fused silica, *J. Opt. Soc. Am.* **55**, 1205 (1965).
- [27] M. Daimon and A. Masumura, Measurement of the refractive index of distilled water from the near-infrared region to the ultraviolet region, *Appl. Opt.* **46**, 3811 (2007).
- [28] S. R. Parnell, A. L. Washington, A. J. Parnell, A. Walsh, R. M. Dalgliesh, F. Li, W. A. Hamilton, S. Prevost, J. P. A. Fairclough, and R. Pynn, Porosity of silica Stöber particles determined by spin-echo small angle neutron scattering, *Soft Matter* **12**, 4709 (2016).